IEEE Access
Multidisciplinary | Rapid Review | Open Access Journal

Received June 13, 2020, accepted July 23, 2020, date of publication August 3, 2020, date of current version August 21, 2020.

Digital Object Identifier 10.1109/ACCESS.2020.3013897

A New Approach Integrated Magnetics Double-Frequency DC/DC Converter

SHENGWEI GAO AND HAO WANG
Tianjin Key Laboratory of Advanced Technology of Electrical Engineering and Energy, Tiangong University, Tianjin 30038, China
School of Electrical Engineering and Automation, Tiangong University, Tianjin 300387, China

Corresponding author: Hao Wang (haowang951@126.com)

This work was supported in part by the National Natural Science Foundation of China (NSFC) under Grant 51807139, in part by the Natural Science Foundation of Tianjin under Grant 19JCQNJC03600, and in part by the Graduate Research and Innovation Project of Tianjin under Grant 2019YJSS026.

ABSTRACT Double-frequency DC/DC converter can improve switching frequency and reduce switching loss than single-frequency DC/DC converter. However, it is heavy and large due to its small high-frequency inductor and large low-frequency inductor. In this article, based on the study on the magnetic integration of the double-frequency DC/DC converter, a novel magnetic integration method was proposed to integrate two inductors with different working frequencies into an EE magnetic core. The proposed magnetic integration scheme is attractive: It outperforms the discrete magnetic double-frequency DC/DC converter in the weight and volume reduction of the magnetic components, the power density improvement of the converter and cost reduction. Compared with the existing solutions of integrated magnetic double-frequency DC/DC converter, this method can further increase the power density of the converter, and reduce the saturation of the magnetic integration components, thereby reducing the iron core loss, as well as improving the dynamic response of the low frequency cell and hence reduce the switching loss. A 150W integrated magnetic double-frequency DC/DC converter was made based on the proposed method, which has been verified by experiments.

INDEX TERMS Magnetic integration inductors, double-frequency dc/dc converter, current shunt to reduce loss, efficiency, dynamic response, gyrator-capacitor model, finite element analysis.

I. INTRODUCTION

With the rapid development of power electronics technology, DC/DC converters have been widely used in various fields and developing towards higher frequency and higher power density [1]. However, the switching loss will increase with the increase of the switching frequency, which will decrease the efficiency and reliability of the converter. To effectively resolve the contradiction between high frequency and high switching losses, double-frequency DC/DC converter has been developed, which can obtain high-frequency output performance with low-frequency switching losses. Due to its outstanding performance, double-frequency DC/DC converter has a broad application prospect in the fields of communication power supply, active power filter (APF), voltage regulation module (VRM), and so on. The double-frequency buck converter (DF-BC) proposed in reference [2] is shown in figure 1. In [3], the influence of the parameters of DF-BC on the system performance was studied in detail.

The associate editor coordinating the review of this manuscript and approving it for publication was Pierluigi Siano.

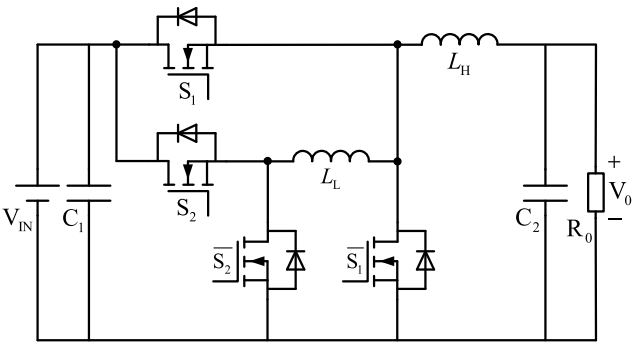

FIGURE 1. Double-frequency buck converter.

In reference [4], the basic DF-BC, basic double-frequency boost converter, and basic double-frequency buck-boost converter were deduced based on the double-frequency switch-inductor rotating three-terminal network.

However, according to statistics, the weight and the volume of magnetic components (including inductors and transformers, etc.) generally account for 30%-40% and 20%-30% of

the total weight and volume of a converter, respectively. Especially for a power supply with high-frequency operation and modular design, the proportions of weight and volume of magnetic components will be even higher [5]. To resolve this issue, integrated magnetics (IM) technology has been developed, which can effectively reduce the volume, weight, cost, and loss of magnetic components. A basic double-frequency converter is usually heavy and large due to its small high-frequency inductor and large low-frequency inductor. Therefore, for double-frequency converters, it is of great significance to integrate the two inductors with different working frequencies [6].

In this article, a new type of integrated magnetic double-frequency converter was proposed. The electric circuit-magnetic circuit coupling principle of the new magnetic integrated inductor is analyzed. The electric circuit-magnetic circuit coupling principle of the novel integrated magnetic inductors was analyzed. The design principle of the inductors and the dynamic performance simulation results of different magnetic components were compared through a gyrator-capacitor model. The finite element model of the magnetic components was established to verify the distribution of magnetic flux density and magnetic field strength in different magnetic components. Compared with the existing inter-inductor magnetic integration schemes, the proposed method has a lower magnetic core saturation and magnetic field strength, a faster dynamic performance of the low-frequency cell, and a better shunt effect, reducing the weight and volume of the magnetic components of the double-frequency converter.

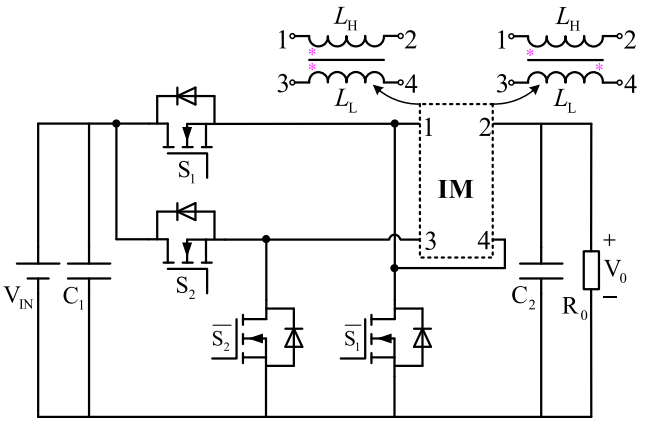

FIGURE 2. Directly couple of the two inductors.

II. MAGNETIC INTEGRATION METHOD AND PRINCIPLE ANALYSIS

A. INTEGRATED MAGNETICS INDUCTOR METHOD

There are two modes of direct coupling integration between two inductors: the one is connection by the same end, and the other is connection by different ends [7], as shown in figure 2. This integration method can reduce the output current ripple, and even achieve zero ripple through a reasonable design. When the two inductors work at different frequencies, the low-frequency voltage and the high-frequency voltage are coupled on the high-frequency and low-frequency inductors respectively, so that the high-frequency switching current stress increases and the two inductors cannot work normally, weakening the original advantages of double-frequency structure and greatly decreasing output performance and efficiency of the converter.

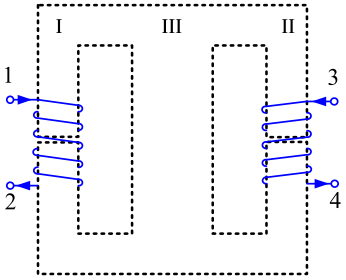

FIGURE 3. Provide a low reluctance magnetic circuit.

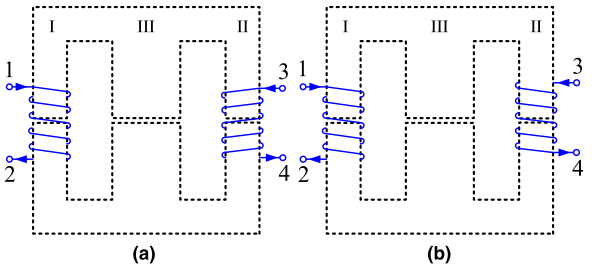

FIGURE 4. Forward and reverse coupling magnetic integration. (a) Forward coupling. (b) Reverse coupling.

In [8], a general inductor magnetic integration method was proposed to decouple magnetic integration through a low-resistance magnetic circuit, as shown in figure 3. A similar method can be used to decouple integration among multiple magnetic components (including inductors and transformers) [9]. In literature [10], an integration method of forward coupling and reverse coupling was proposed for multichannel interleaved parallel converters, as shown in figure 4. However, neither of these two methods can be applied to a double-frequency converter due to its two inductors' great differences in inductance value and working frequency, which lead to the great magnetic flux difference between the two inductors and the uneven distribution of the magnetic flux accordingly. In order to avoid none of the three magnetic poles from saturation, the magnetic core should be selected according to the magnetic column with the highest magnetic flux density. In this way, the utilization rate of the magnetic core will be greatly reduced, and the volume of the final selected magnetic core may be larger than the sum of the volumes of the discrete inductive magnetic cores.

In literature [11], a decoupling integrated magnetics (DIM) method by counteracting the coupling effect was proposed, as shown in figure 5, and applied to the magnetic integrations between inductor and transformer as well as between transformer and transformer. In [12], this decoupling integration

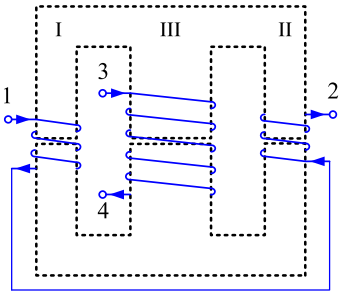

FIGURE 5. Counteract coupling magnetic integration.

method was applied to DF-BC to implement the magnetic integration of two inductors working at different frequencies. Although this method has achieved the magnetic integration of high-frequency inductor and low-frequency inductor in one EE magnetic core, it will reduce the dynamic performance of low-frequency cell according to the following analysis in this article. In addition, regardless of the type of converter, this magnetic integration method will make the side column II of magnetic core easy to saturate, resulting in serious heating of the magnetic core and affecting the operation of the converter.

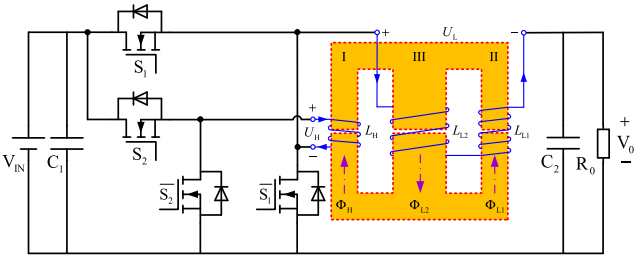

FIGURE 6. NIM double-frequency buck converter.

In order to solve the above problems, based on the DF-BC example, a novel integrated magnetics (NIM) method suitable for double-frequency DC/DC converter was proposed in this article, to integrate two inductors with different working frequencies into one EE magnetic core, as shown in figure 6. Compared with the prior art solutions, his method can solve the problem that side column II of magnetic core is easy to be saturated, reduce the magnetic saturation of the integrated magnetics, improve the utilization rate of the magnetic core, and thus reduce the core loss of the converter. On the one hand, it can further reduce the volume of magnetic components and increase the power density of the converter; on the other hand, it can improve the dynamic response speed of the low-frequency cell of the double-frequency converter, and thus improve the shunt effect of the integrated magnetic double-frequency converter.

B. ANALYSIS OF NIM INDUCTORS ELECTRIC CIRCUIT-MAGNETIC CIRCUIT COUPLING PRINCIPLE

Figure 7 shows the structure of NIM inductors. L_H is a high-frequency inductor, L_{L1} is a low-frequency inductor wound

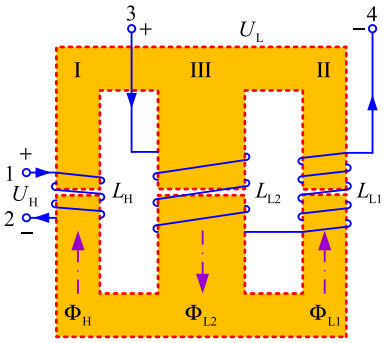

FIGURE 7. NIM inductors structure.

on the column II of the magnetic core, and L_{L2} is a low-frequency inductor wound on the column III of the magnetic core. U_H and U_L are the voltages across the high-frequency inductor and the low-frequency inductor respectively. Φ_H is the magnetic flux generated by the high-frequency inductor, Φ_{L1} is the magnetic flux generated by the low-frequency inductor wound on the column II of magnetic core II, and Φ_{L2} is the magnetic flux generated by the low-frequency inductor wound on the column III of magnetic core. Figure 8 shows the NIM equivalent magnetic circuit [13]. N_H is the number of turns of the high-frequency inductor, N_{L1} is the number of turns of the low-frequency inductor wound on the column II of magnetic core, and N_{L2} is the number of turns of the low-frequency inductor wound on the column II of magnetic core. $N_H i_H$ is the MMF generated by the high-frequency inductor winding, $N_{L1} i_L$ is the MMF generated by the winding of low-frequency inductor wound on the column II of magnetic core, and $N_{L2} i_L$ is the MMF generated by the low frequency inductor wound on the core III column winding, and $N_{L2} i_L$ is the MMF generated by the winding of low-frequency inductor wound on the column III of magnetic core. R_1, R_2 and R_3 are the equivalent reluctances of the columns I, II and III respectively. Φ_1, Φ_2 and Φ_3 are the magnetic fluxes produced by windings under the joint action of the columns I, II and III of the magnetic core respectively.

To facilitate design, air gaps of three columns of EE magnetic core are open at the same time. According to Ohm law of the magnetic circuit, the magnetic flux generated by each winding is:

$$\begin{cases} \Phi_H = \dfrac{N_H i_H}{R_1 + R_2 // R_3} = N_H i_H \dfrac{R_2 + R_3}{\Delta} \\ \Phi_{L1} = \dfrac{N_{L1} i_L}{R_2 + R_1 // R_3} = N_{L1} i_L \dfrac{R_1 + R_3}{\Delta} \\ \Phi_{L2} = \dfrac{N_{L2} i_L}{R_3 + R_1 // R_2} = N_{L2} i_L \dfrac{R_1 + R_2}{\Delta} \end{cases} \quad (1)$$

In formula (1), $\Delta = R_1R_2 + R_1R_3 + R_2R_3$. According to figure 8, the magnetic fluxes produced by each windings under the joint action of the columns I, II and III of magnetic

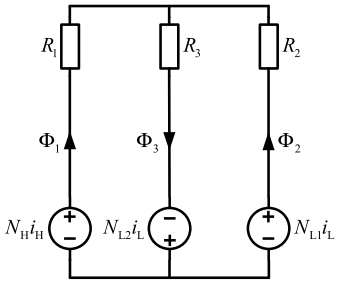

FIGURE 8. NIM equivalent magnetic circuit.

core are as follows:

$$\begin{cases} \Phi_1 = \Phi_H - \Phi_{L1}\dfrac{R_3}{R_1+R_3} + \Phi_{L2}\dfrac{R_2}{R_1+R_2} \\ \Phi_2 = -\Phi_H\dfrac{R_3}{R_2+R_3} + \Phi_{L1} + \Phi_{L2}\dfrac{R_1}{R_1+R_2} \\ \Phi_3 = \Phi_H\dfrac{R_2}{R_2+R_3} + \Phi_{L1}\dfrac{R_1}{R_1+R_3} + \Phi_{L2} \end{cases} \tag{2}$$

Substituting formula (1) into formula (2) to obtain

$$\begin{cases} \Phi_1 = N_H i_H\dfrac{R_2+R_3}{\Delta} - N_{L1} i_L\dfrac{R_3}{\Delta} + N_{L2} i_L\dfrac{R_2}{\Delta} \\ \Phi_2 = -N_H i_H\dfrac{R_3}{\Delta} + N_{L1} i_L\dfrac{R_1+R_3}{\Delta} + N_{L2} i_L\dfrac{R_1}{\Delta} \\ \Phi_3 = N_H i_H\dfrac{R_2}{\Delta} + N_{L1} i_L\dfrac{R_1}{\Delta} + N_{L2} i_L\dfrac{R_1+R_2}{\Delta} \end{cases} \tag{3}$$

According to Faraday's law of electromagnetic induction, the voltage U_H across the high-frequency inductor and the voltage U_L across the low-frequency inductor can be obtained as follows:

$$\begin{cases} U_H = N_H\dfrac{d\Phi_1}{dt} \\ U_L = N_{L1}\dfrac{d\Phi_2}{dt} + N_{L2}\dfrac{d\Phi_3}{dt} \end{cases} \tag{4}$$

Substituting equation (3) into equation (4) to obtain:

$$\begin{bmatrix} U_H \\ U_L \end{bmatrix} = \begin{bmatrix} L_{HH} & M_{HL} \\ M_{LH} & L_{LL} \end{bmatrix} \begin{bmatrix} \dfrac{di_H}{dt} \\ \dfrac{di_L}{dt} \end{bmatrix} \tag{5}$$

The specific parameters of the matrix of formula (5) are shown in formula (6).

$$\begin{cases} L_{HH} = \dfrac{N_H^2(R_2+R_3)}{\Delta} \\ L_{LL} = \dfrac{N_{L1}^2(R_1+R_3) + 2N_{L1}N_{L2}R_1 + N_{L2}^2(R_1+R_2)}{\Delta} \\ M_{HL} = \dfrac{N_H(N_{L2}R_2 - N_{L1}R_3)}{\Delta} \\ M_{LH} = \dfrac{N_H(-N_{L1}R_3 + N_{L2}R_2)}{\Delta} \end{cases} \tag{6}$$

When the low-frequency inductor winding mode is $N_{L1}/R_2 = N_{L2}/R_3$, it also the following formula is satisfied:

$$N_{L1}R_3 = N_{L2}R_2 \tag{7}$$

TABLE 1. The table of switch mode.

Mode	S_1	S_2	$\bar{S}_1$	$\bar{S}_2$
(a)	ON	ON	OFF	OFF
(b)	OFF	ON	ON	OFF
(c)	ON	OFF	OFF	ON
(d)	OFF	OFF	ON	ON

Substituting formula (7) into formula (5) to obtain formula (8):

$$\begin{bmatrix} U_H \\ U_L \end{bmatrix} = \begin{bmatrix} L_{HH} & 0 \\ 0 & L_{LL} \end{bmatrix} \begin{bmatrix} \dfrac{di_H}{dt} \\ \dfrac{di_L}{dt} \end{bmatrix} \tag{8}$$

According to equation (8), it can be clearly seen that the coupling coefficient between the high-frequency inductor and the low-frequency inductor $M_{HL} = M_{LH} = 0$. Therefore, this method has completely decoupled the two inductors with different frequencies.

Assuming that the magnetic resistance of the EE core satisfies the formula (9), and the formula (9) is substituted into the formula (7) to obtain the formula (10):

$$R = R_3 = R_1/2 = R_2/2 \tag{9}$$

$$N_{L1} = 2N_{L2} = 2N_L \tag{10}$$

Substituting formula (9) and formula (10) into formula (8) to obtain formula (11):

$$\begin{bmatrix} U_H \\ U_L \end{bmatrix} = \begin{bmatrix} \dfrac{3N_H^2}{8R} & 0 \\ 0 & \dfrac{3N_L^2}{R} \end{bmatrix} \begin{bmatrix} \dfrac{di_H}{dt} \\ \dfrac{di_L}{dt} \end{bmatrix} \tag{11}$$

According to the above analysis, when the winding parameters of the low-frequency inductor winding satisfy equation (7), the external characteristics of the high-frequency and low-frequency inductors will not affect each other, and the complete decoupling of the two inductors will be realized.

III. ANALYSIS AND DESIGN OF NIM INDUCTORS

A. ANALYSIS OF NIM DOUBLE-FREQUENCY BUCK CONVERTER

Supposing the operating frequency of the high-frequency cell is f_H and the operating frequency of the low-frequency cell is f_L, then

$$f_H = n \cdot f_L \tag{12}$$

One switching period T_L of the low-frequency cell includes n high-frequency switching periods T_H, which means that there are four switching states in a low-frequency switching period, as shown in table 1.

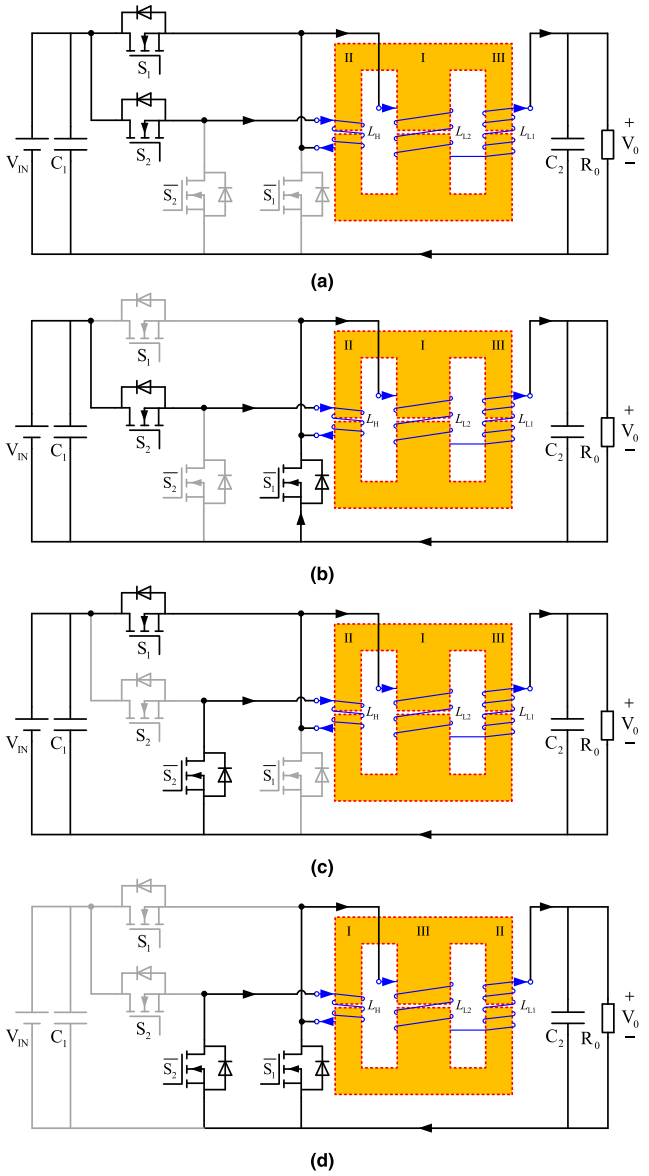

FIGURE 9. NIM operation mode of double-frequency buck converter. (a) Mode a. (b) Mode b.(c) Mode c.(d) Mode d.

Figure 9 shows the operation mode of the NIM DF-BC [6]. Mode (a): as shown in figure 9 (a), the voltage across the high-frequency inductor is positive, and the high-frequency inductor current i_H is rising at this time; the low-frequency inductor is short-circuited by the switch S_1, so the low-frequency inductor current i_L remains unchanged. Mode (b): as shown in figure 9 (b), the voltage across the high-frequency inductor is negative, and the high-frequency inductor current i_H is falling at this time; the voltage across the low-frequency inductor is positive, and the low-frequency inductor current i_L is rising at this time. Mode (c): as shown in figure 9 (c), the voltage across the high-frequency inductor is positive, and the high-frequency inductor current i_H is rising at this time; the voltage across the low-frequency inductor is negative, and the low-frequency inductor current i_L is falling at this time. Mode (d): as shown in figure 9 (d), the voltage across the high-frequency inductor is negative, the high-frequency inductor current i_H is falling at this time; the low-frequency inductor is short-circuited by the switch tub $\bar{S}_1$, and the low-frequency inductor current i_L remains unchanged. The voltage waveforms and current change rates of high-frequency and low-frequency inductors under four modes are shown in table 2.

TABLE 2. The inductor waveform in different modes.

Mode	V_{L_H}	di_{L_H}/dt	V_{L_L}	di_{L_L}/dt
(a)	$V_{IN}-V_0$	$(V_{IN}-V_0)/L_H$	0	0
(b)	V_0	$-V_0/L_H$	V_{IN}	V_{IN}/L_L
(c)	$V_{IN}-V_0$	$(V_{IN}-V_0)/L_H$	$-V_{IN}$	$-V_{IN}/L_L$
(d)	V_0	$-V_0/L_H$	0	0

TABLE 3. Flux-rate of three magnetic columns in different modes.

Mode	$\dot{\Phi}_H$	$\dot{\Phi}_{L1}$	$\dot{\Phi}_{L2}$
(a)	$(V_{IN}-V_0)/N_H$	0	0
(b)	$-V_0/N_H$	$V_{IN}N_{L1}/(N_{L1}+N_{L2})$	$V_{IN}N_{L2}/(N_{L1}+N_{L2})$
(c)	$(V_{IN}-V_0)/N_H$	$-V_{IN}N_{L1}/(N_{L1}+N_{L2})$	$-V_{IN}N_{L2}/(N_{L1}+N_{L2})$
(d)	$-V_0/N_H$	0	0

Based on figure 9, table 1 and table 2, table 3 is obtained. The duty cycles of the high-frequency cell and the low-frequency cell are supposed as D_H and D_L respectively. In the steady state, according to the volt-second balance principle, the change rate of magnetic flux on each magnetic column in one period is zero. Therefore, for Φ_H:

$$\frac{V_{IN}-V_0}{N_H}D_H-\frac{V_0}{N_H}(1-D_H)=0 \tag{13}$$

Simplified formula (13) can be obtained as follows:

$$V_{IN}D_H=V_0 \tag{14}$$

From equations (13) and (14), it can be seen that the voltage transmission ratios of the NIM inductors and the discrete magnetics(DM) inductor are the same. This integration method has no effect on the operation state of the converter.

For $\Phi_{L1}(\Phi_{L2}$ similarly), we can obtain:

$$\frac{(1-D_H)D_LV_{IN}N_{L1}}{N_{L1}+N_{L2}}-\frac{D_H(1-D_L)V_{IN}N_{L1}}{N_{L1}+N_{L2}}=0 \tag{15}$$

Simplified formula (15) can be obtained as follows:

$$D_H=D_L \tag{16}$$

From equations (15) and (16), it can be seen that the duty cycle of the high-frequency and low-frequency switches with

integrated inductors is equal in the steady-state operation. The duty cycles of the high-frequency and low-frequency switches of the discrete inductors obtained from the literature [6] are the same. Therefore, the integration method can adopt the same control mode as the discrete inductors.

For high-frequency inductor current, according to the law of electromagnetic induction and Ohm law of magnetic circuit, it can be deduced that:

$$\frac{\mathrm{d}i_{\mathrm{H}}}{\mathrm{d}t}=\frac{\mathrm{d}(F_{\mathrm{H}}/N_{\mathrm{H}})}{\mathrm{d}t}=\frac{\mathrm{d}(\Phi_{\mathrm{H}}\cdot R_{\mathrm{H}})}{N_{\mathrm{H}}\mathrm{d}t}=\frac{R_{\mathrm{H}}U_{\mathrm{H}}}{N_{\mathrm{H}}^2}=\frac{U_{\mathrm{H}}}{L_{\mathrm{H}}} \tag{17}$$

In the formula (17): $R_{\mathrm{H}}=R_1+R_2//R_3$.

For low-frequency inductor current, according to the law of electromagnetic induction and Ohm law of magnetic circuit, it can be deduced that:

$$\frac{\mathrm{d}i_{\mathrm{L}}}{\mathrm{d}t}=\frac{\mathrm{d}[F_{\mathrm{L}}/(N_{\mathrm{L1}}+N_{\mathrm{L2}})]}{\mathrm{d}t} \tag{18}$$

$$F_{\mathrm{L}}=(\Phi_{\mathrm{L1}}+\Phi_{\mathrm{L2}})\cdot(R_2+R_3) \tag{19}$$

Substituting equation (19) into equation (18) to obtain:

$$\frac{\mathrm{d}i_{\mathrm{L}}}{\mathrm{d}t}=\frac{(R_2+R_3)U_{\mathrm{L}}}{(N_{\mathrm{L1}}+N_{\mathrm{L2}})^2}=\frac{U_{\mathrm{L}}}{L_{\mathrm{L}}} \tag{20}$$

It can be seen that the current ripple of the high-frequency inductor is related to $L_{\mathrm{H}}=N_{\mathrm{H}}^2/R_{\mathrm{H}}$, that repres-ents the size of the inductor. $L_{\mathrm{L}}=(N_{\mathrm{L1}}+N_{\mathrm{L2}})^2/(R_2+R_3)$ is the size of the inductor value, and the current ripple of the low-frequency inductor is related to it, which is consistent with the discrete inductors.

As analyzed before, the voltage, current and magnetic flux waveforms of NIM in one switching cycle shown in figure 10 can be obtained [14], [15].

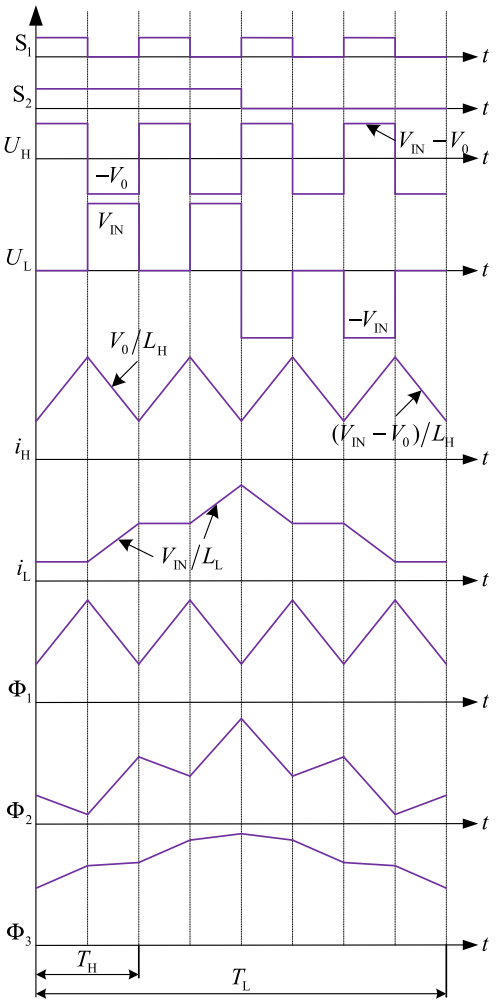

FIGURE 10. Voltage, current and flux waveforms of one switching period of NIM.

B. DETERMINATION OF TURNS AND AIR GAP OF NIM INDUCTORS

Figure 11 shows the air gap and cross-sectional area diagram of NIM, where l_{g} is the air gap length of the magnetic core. A_{I}, A_{II}, and A_{III} are the cross-sectional areas of the two side columns and the middle column of the magnetic core respectively. Figure 12 shows an equivalent gyrator-capacitor model of NIM, where C_{I}, C_{II} and C_{III} are the equivalent magnetic conductances of the two side columns and the middle column of the magnetic core respectively, $C_{\mathrm{g_I}}$, $C_{\mathrm{g_{II}}}$, and $C_{\mathrm{g_{III}}}$ are the equivalent magnetic permeabilities of the air gaps on both sides of the column and the equivalent magnetic permeability of the air gap in the middle of the column respectively, N_{H} is the number of turns of the high-frequency inductors, N_{L1} and N_{L2} are the number of turns of the low-frequency inductors wound on the column II and column III of the magnetic core.

$$L_{\mathrm{H}}=N_{\mathrm{H}}^2\left\{(C_{\mathrm{I}}//C_{\mathrm{g_I}})//\left[(C_{\mathrm{II}}//C_{\mathrm{g_{II}}})+(C_{\mathrm{III}}//C_{\mathrm{g_{III}}})\right]\right\} \tag{21}$$

$$L_{\mathrm{L}}=(N_{\mathrm{L1}}+N_{\mathrm{L2}})^2\left[(C_{\mathrm{II}}//C_{\mathrm{g_{II}}})//(C_{\mathrm{III}}//C_{\mathrm{g_{III}}})\right] \tag{22}$$

For the sake of simplicity of analysis, we do not consider scattered magnetic flux for the time being. Among them: $C_{\mathrm{g_I}}=\mu_0A_{\mathrm{I}}/l_{\mathrm{g}}$, $C_{\mathrm{g_{II}}}=\mu_0A_{\mathrm{II}}/l_{\mathrm{g}}$, $C_{\mathrm{g_{III}}}=\mu_0A_{\mathrm{III}}/l_{\mathrm{g}}$, $C_{\mathrm{I}}=\mu_{\mathrm{r}}A_{\mathrm{I}}/l_{A_{\mathrm{I}}}$, $C_{\mathrm{II}}=\mu_{\mathrm{r}}\mu_0A_{\mathrm{II}}/l_{A_{\mathrm{II}}}$, $C_{\mathrm{III}}=\mu_{\mathrm{r}}\mu_0A_{\mathrm{III}}/l_{A_{\mathrm{III}}}$, μ_0 is the magn-etic permeability in vacuum. Due to $\mu_{\mathrm{r}}\gg\mu_0$, the air gap magnetic permeability is much smaller than the magnetic core magnetic flux permeability μ_{r}, so the high and low frequency inductances can be simplified as:

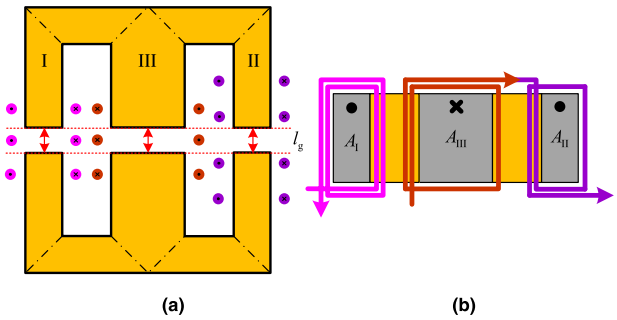

FIGURE 11. Air gap and sectional area of NIM. (a) Magnetic core air gap. (b)Cross sectional area of magnetic core.

$$L_{\mathrm{H}}=N_{\mathrm{H}}^2\left[C_{\mathrm{g_I}}//(C_{\mathrm{g_{II}}}+C_{\mathrm{g_{III}}})\right] \tag{23}$$

$$L_{\mathrm{L}}=(N_{\mathrm{L1}}+N_{\mathrm{L2}})^2(C_{\mathrm{g_{II}}}//C_{\mathrm{g_{I\,II}}}) \tag{24}$$

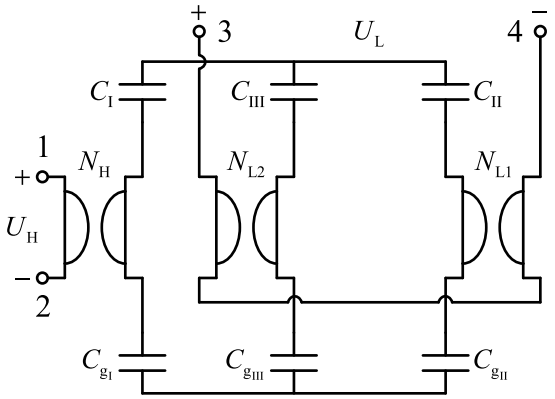

FIGURE 12. Equivalent gyrator-capacitor model of NIM.

Then we can obtain:

$$L_H = N_H^2 \frac{\mu_0 A_I (A_{II} + A_{III})}{l_g (A_I + A_{II} + A_{III})} \tag{25}$$

$$L_L = (N_{L1} + N_{L2})^2 \frac{\mu_0 A_{II} A_{III}}{l_g (A_{II} + A_{III})} \tag{26}$$

Because the three windings share the window area of the magnetic core, in order to verify whether the three windings can be wound on the EE magnetic core, there should be:

$$A_W \geq \max \left\{ \frac{N_H r_H^2 + N_{L2} r_{L2}^2}{K_u}, \frac{N_{L1} r_{L1}^2 + N_{L2} r_{L2}^2}{K_u} \right\} \tag{27}$$

In the formula (27):

r_H, r_{L1}, r_{L2}—wire radius of corresponding winding;

K_u− the filling coefficient of the winding.

C. THE MAXIMUM FLUX DENSITY OF THE MAGNETIC COLUMN OF NIM

For the magnetic column I where the high-frequency inductor is located, the two magnetic columns of the low-frequency inductor will not affect the magnetic column I by rationally designing the number of turns of the low-frequency inductor. So the maximum magnetic flux density of magnetic column I is:

$$B_{I,max} = \frac{L_H i_{H,max}}{N_H A_I} \tag{28}$$

The minimum flux density of column I is:

$$B_{I,min} = \frac{L_H i_{H,min}}{N_H A_I} \tag{29}$$

The maximum and minimum magnetic flux densities of magnetic column II generated by the winding on magnetic column II are as follows:

$$\Delta B_{II,max} = \frac{L_L i_{L,max}}{(N_{L1} + N_{L2}) A_{II}} \tag{30}$$

$$\Delta B_{II,min} = \frac{L_L i_{L,min}}{(N_{L1} + N_{L2}) A_{II}} \tag{31}$$

Similarly, the maximum and minimum magnetic flux densities of magnetic column III generated by the winding on magnetic column III are as follows:

$$\Delta B_{III,max} = \frac{L_L i_{L,max}}{(N_{L1} + N_{L2}) A_{III}} \tag{32}$$

$$\Delta B_{III,min} = \frac{L_L i_{L,min}}{(N_{L1} + N_{L2}) A_{III}} \tag{33}$$

According to the superposition theorem, the absolute values of the maximum magnetic flux densities of magnetic columns II and III can be obtained as:

$$\begin{aligned} B_{II,max} &= \Delta B_{II,max} + \Delta B_{III,max} - B_{I,min} \\ &= \frac{L_L i_{L,max}}{(N_{L1} + N_{L2})} \left(\frac{1}{A_{II}} + \frac{1}{A_{III}} \right) - \frac{L_H i_{H,min}}{N_H A_I} \end{aligned} \tag{34}$$

$$\begin{aligned} B_{III,max} &= \Delta B_{II,max} + \Delta B_{III,max} + B_{I,max} \\ &= \frac{L_L i_{L,max}}{(N_{L1} + N_{L2})} \left(\frac{1}{A_{II}} + \frac{1}{A_{III}} \right) + \frac{L_H i_{H,max}}{N_H A_I} \end{aligned} \tag{35}$$

The above-derived formulas can be used to verify whether local magnetic columns will be saturated when designing NIM.

D. COMPARISON OF DIFFERENT MAGNETICS

As the core material is selected, the maximum saturation magnetic flux density of the magnetic core is determined accordingly. In order to ensure the normal and efficient operation of the converter, the maximum working magnetic flux density of each magnetic column of the magnetic core shall not exceed its saturation magnetic flux. For inductors, the maximum operating flux density is:

$$B_{max} = \frac{L I_{max}}{N A_e} \tag{36}$$

In [12]: according to formula (36), using NA_e to characterize the volume of the magnetic part, the magnetic chain $\psi = LI$ is proportional to the size of the magnetic components. Therefore, the magnetic links of the magnetic components can be used to indirectly compare the sizes of discrete magnetics(DM), decoupled integrated magnetics(DIM) and new integrated magnetics(NIM).

For EE type magnetic core, the cross-sectional area of the middle column is approximately equal to twice that of the side column, and the equivalent magnetic permeance of the middle column is nearly twice that of the side column. In order to facilitate the analysis, the equivalent magnetic conductivity of the middle column is taken as twice that of the side column.

The comparison results are shown in table 4. According to the following prototype data: $L_H = 200$uH, $L_L = 800$uH, $i_{Hmax} = 6$A, $i_{Lmax} = 3$A. The prototype data is substituted into table 4 to obtain table 5.

It can be seen from table 4 and table 5: compared with DM, the maximum magnetic flux linkage values of magnetic columns A_I and A_{III} are significantly reduced by using DIM, and the maximum magnetic flux linkage value of magnetic column A_{II} is equivalent to that before integration, so the volume of DIM can be effectively reduced compared with

TABLE 4. The ψ_{max} comparison.

Mode	Magnetic core A_{I}	Magnetic core A_{II}	Magnetic core A_{III}
DM	$0.5(L_{\mathrm{L}}i_{\mathrm{L\,max}}+L_{\mathrm{H}}i_{\mathrm{H\,max}})$	$0.5(L_{\mathrm{L}}i_{\mathrm{L\,max}}+L_{\mathrm{H}}i_{\mathrm{H\,max}})$	$L_{\mathrm{L}}i_{\mathrm{L\,max}}+L_{\mathrm{H}}i_{\mathrm{H\,max}}$
DIM	$0.5(L_{\mathrm{H}}i_{\mathrm{H\,max}}-L_{\mathrm{L}}i_{\mathrm{L\,min}})$	$0.5(L_{\mathrm{L}}i_{\mathrm{L\,max}}+L_{\mathrm{H}}i_{\mathrm{H\,max}})$	$L_{\mathrm{L}}i_{\mathrm{L\,max}}$
NIM	$L_{\mathrm{H}}i_{\mathrm{H\,max}}$	$(2L_{\mathrm{L}}i_{\mathrm{L\,max}}-L_{\mathrm{H}}i_{\mathrm{H\,min}})/3$	$(L_{\mathrm{L}}i_{\mathrm{L\,max}}+2L_{\mathrm{H}}i_{\mathrm{H\,max}})/3$

TABLE 5. The value of ψ_{max}.

Mode	Magnetic core A_{I}	Magnetic core A_{II}	Magnetic core A_{III}
DM	1.8×10^{-3} Wb	1.8×10^{-3} Wb	3.6×10^{-3} Wb
DIM	-0.3×10^{-3} Wb	1.8×10^{-3} Wb	1.8×10^{-3} Wb
NIM	1.2×10^{-3} Wb	1.2×10^{-3} Wb	1.6×10^{-3} Wb

that of DM. Compared with DM, the maximum magnetic flux linkage values of magnetic columns A_{I}, A_{II} and A_{III} are significantly reduced by using NIM, so the volume of NIM can be effectively reduced compared with that of DM. By comparison with DIM, NIM increases the maximum magnetic flux linkage value of column A_{I} by three times, reduces the maximum flux value of column A_{II} to $2/3$, and makes the maximum magnetic flux linkage value of magnetic column A_{III} is close to that of DIM but still smaller than its value. Although the maximum magnetic flux linkage value of NIM magnetic column A_{I} is three times that of DIM, the maximum magnetic flux linkage values of magnetic column A_{II} and A_{III} of DIM are both greater than those of NIM, so the magnetic core should be selected according to the maximum magnetic flux linkage value of the side column. The maximum magnetic flux linkage value of the NIM side column A_{I} is equal to the maximum magnetic flux linkage value of the magnetic column A_{II}. Although the maximum magnetic flux linkage value of the magnetic column A_{III} is large, the cross-sectional area of the core A_{e} in the core of the EE core is very large. Therefore, the magnetic core of NIM should be selected according to the maximum magnetic flux linkage value of the middle column. As a result, the magnetic core volume of NIM can be effectively reduced compared with that of DIM.

When the magnetic core is running, the magnetic flux linkages generated by the magnetic columns A_{I}, A_{II}, and A_{III} in the DIM integration mode will be superimposed on the magnetic column A_{II}, so that the magnetic column A_{II} is easy to saturate. Therefore, the magnetic core should be selected according to the side column during the design. However, in the NIM integration method, the magnetic flux linkages generated by magnetic columns A_{I}, A_{II}, and A_{III} will be superimposed on magnetic column A_{III}, but the cross-sectional area A_{e} of magnetic column A_{III} is larger than the cross-sectional area A_{e} of magnetic column A_{I} and magnetic column A_{II}. which leads to a low magnetic flux linkage density of the magnetic column A_{III}. Therefore, it is necessary to select the magnetic core according to the middle column during design.

For the same type of magnetic cores, the maximum working magnetic density of the NIM magnetic core is lower than that of the DIM magnetic core, so a smaller magnetic core can be selected for NIM to further reduce the volume of the integrated magnetic inductors.

IV. SIMULATION OF NEW INTEGRATED INDUCTOR

A. SIMULATION COMPARISON OF GYRATOR-CAPACITOR MODEL FOR MAGNETIC COMPONENTS

The gyrator-capacitor model [16], [17] is suitable for simulation modeling due to its advantages, such as conve-nient modeling, complete electromagnetic information and suitable for hybrid simulation of electric-magnetic system. In order to verify the performance of different magnetic components, an equivalent model of magnetic components was established by using PSpice to compare DF-BC closed-loop simulations of DM, DIM, and NIM through Simulink and PSpice co-simulation, as shown in figure 13.

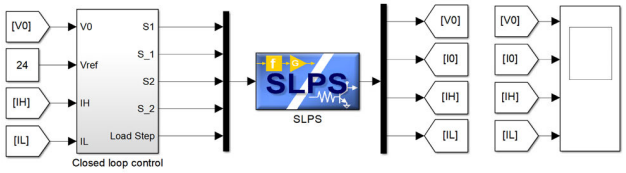

FIGURE 13. Simulink/PSpice co-simulation.

The simulation parameters are as follows: input DC voltage $V_{\mathrm{IN}} = 48\mathrm{V}$, output voltage $V_0 = 24\mathrm{V}$, output capacitance $C_2 = 300\mu F$, load current $I_0 = 6\mathrm{A}$, high-frequency switching frequency $f_{\mathrm{H}} = 100\mathrm{kHz}$,low-frequency switching frequenc $f_{\mathrm{L}} = 25\mathrm{kHz}$,high-frequency inductor $L_{\mathrm{H}} = 200\mathrm{uH}$, and low-frequency inductor $L_{\mathrm{L}} = 800\mu H$. Through calculation, for the DIM inductor, the number of turns of each magnetic column is taken as: $N_{\mathrm{I}} = N_{\mathrm{II}} = 31$, $N_{\mathrm{III}} = 83$ respectively. For the number of turns of the NIM inductor at each magnetic column: $N_{\mathrm{H}} = 50$, $N_{\mathrm{L1}} = 75$, $N_{\mathrm{L2}} = 29$.

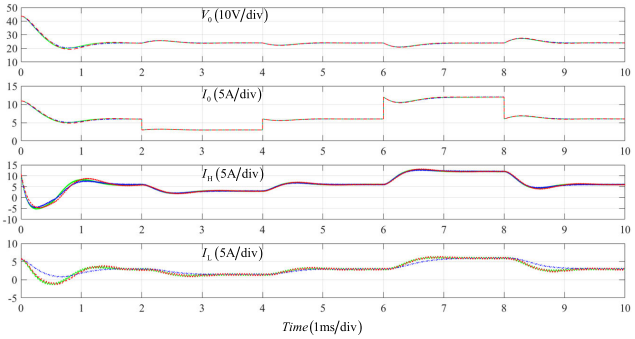

FIGURE 14. Comparison of co-simulation waveform.

Figure 14 shows the closed-loop joint simulation waveforms of DM, DIM and NIM DF-BC under the same

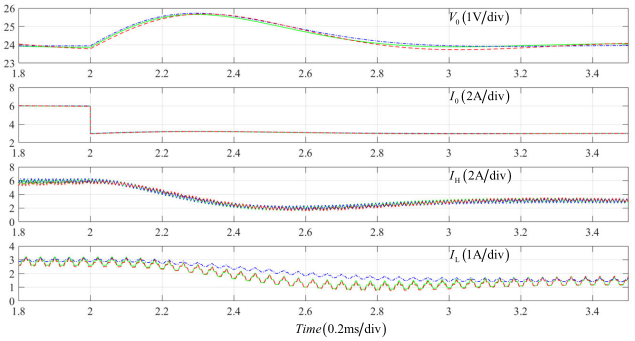

FIGURE 15. Comparison of co-simulation waveform.

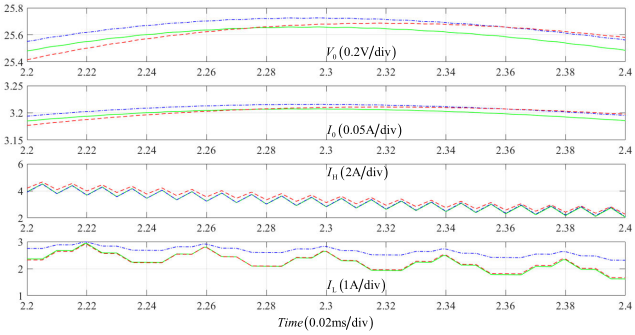

FIGURE 16. Comparison of co-simulation waveform.

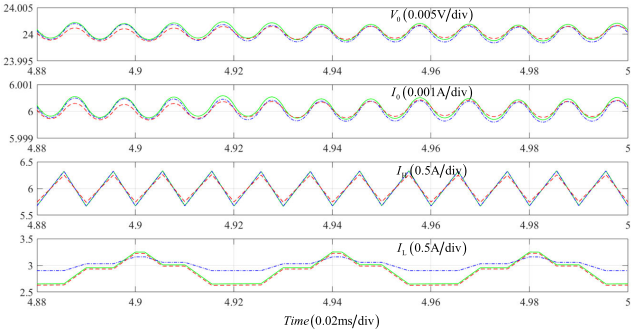

FIGURE 17. Comparison of co-simulation waveform.

compensation condition. Among them, the green waveform represents the simulation waveform of DM, the blue waveform represents the simulation waveform of DIM, and the red waveform represents the simulation waveform of NIM. The output voltage, output current, high-frequency inductor current and low-frequency inductor current were measured respectively. Figure 15 shows the amplification waveforms of the simulation results of figure 14 in the range of 1.8ms to 3.5ms, which is switched to half load in 2ms. Figure 16 shows the further enlarged waveforms of the simulation results of figure 14 from 2.2ms to 2.4ms. Figure 17 shows the steady-state waveforms under full load.

As can be seen in figure 14, the steady-state performance and dynamic performance of the output voltage, output current, high-frequency inductor current, and low-frequency inductor current of the two integration methods are basically the same as those of DM, and both of them can meet the output requirements. In figure 15, it can be seen that the output voltage overshoot of NIM is the largest, followed by DM output voltage overshoot, and that of DIM is the smallest, so the dynamic response speed of NIM is the fastest. It can also be clearly seen in figure 15 that the low-frequency inductor current of DIM has the smallest overshoot and the slowest dynamic response speed, so the response of the DIM low frequency cell to the shunt effect of the high frequency cell slows down. On the one hand, the slowdown of shunting will apply more power to the high-frequency part and affect the response speed of output voltage; on the other hand, the high-frequency part will produce more switching loss. This phenomenon is even more obvious in figure 16.

In figure 16 and figure 17, whether under the static or dynamic condition, the high frequency inductor current of DIM is consistent with that of DM. The low frequency inductor current of DIM has a lower ripple than DM and NIM, but the dynamic response is slower, the low frequency inductance current of NIM is consistent with that of DM. The ripple of high frequency inductance current of NIM is lower than that of DM and NIM, but the dynamic response is unchanged. Under steady-state conditions, the output voltage, output current, and high frequency inductor current ripple of NIM are lower than those of DM and DIM.

In figure 16 and figure 17, whether under the static or dynamic condition, DIM has the consistent current of high-frequency/low-frequency inductor with DM, a lower ripple of low-frequency inductor current than DM and NIM, and a slower dynamic response. NIM has a lower ripple of high-frequency inductor current than DM and NIM, but the unchanged dynamic response. Under a steady-state, NIM has lower output voltage, output current, and high-frequency inductor current ripple than DM and DIM.

To sum up: NIM has the lowest ripple of output voltage, output current and high-frequency inductor current, and the ripple of low-frequency inductor current is the same as that of DM. The dynamic response of NIM's output voltage and output current is the fastest, and the dynamic responses of high-frequency inductor current and low-frequency inductor current are the same as that of DM. The ripple of output voltage, output current and high-frequency inductor current of DIM is the same as that of DM, and the low-frequency inductor current has the lowest ripple.

The dynamic response of the output voltage and output current of DIM is the slowest, the dynamic response of high-frequency inductor current is the same as that of DM, and the dynamic response of low-frequency inductor current is the slowest. Although the low-frequency inductor ripple of DIM is the lowest, its dynamic response speed is sacrificed.

With the magnetic core EE40 of the same size selected, the formula (36) was used to simulate the magnetic flux density of each magnetic column of the two types of inductor magnetic integration components. Figure 18 shows a simulation of the magnetic flux density of each magnetic column

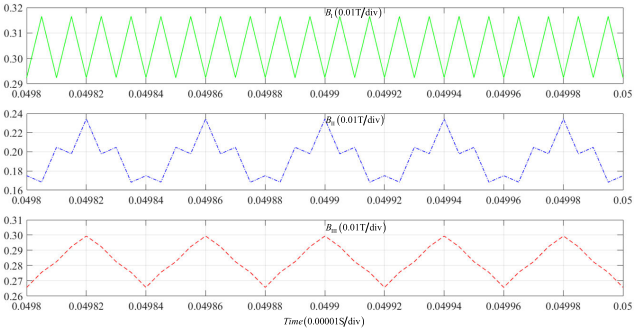

FIGURE 18. NIM magnetic flux density of each column.

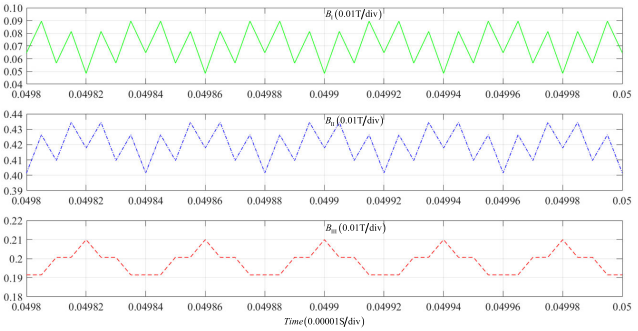

FIGURE 19. DIM magnetic flux density of each column.

of the NIM magnetic core. The peak magnetic flux density of the magnetic column I where the high frequency inductor is located is 0.32T, and the peak magnetic flux density of the magnetic column II where the low frequency inductor is located is 0.235T. The peak magnetic flux density of the magnetic column III is 0.298T. Figure19 shows a simulation of the magnetic flux density of each magnetic column of the DIM magnetic core. The peak magnetic flux density of the magnetic column where the high frequency inductor is located is 0.1T, the peak magnetic flux density of the magnetic column where the high frequency inductor is located is 0.44T, and the peak magnetic flux density of the magnetic column where the low frequency inductor is located is 0.225T. It can be clearly seen from the simulation comparison between figure 18 and figure 19 that the maximum magnetic flux density of the DIM core is 0.44T, which is far beyond the saturated magnetic flux density of 0.35T of the ferrite. The maximum magnetic flux density of the NIM method is 0.32T, which does not reach the saturation flux density. In addition, the magnetic flux densities of the DIM magnetic column I and the magnetic column III are much smaller than the saturation magnetic flux density, so the DIM core side column is easy to saturate, and the utilization rate of the magnetic core is low. For NIM, the magnetic flux density of each magnetic core of the magnetic core is relatively average, and the utilization rate of the magnetic core is higher than that of the DIM method. In the case of selecting the same magnetic core, NIM can work better than DIM, so NIM can further reduce the volume and weight of the magnetic components than DIM.

B. THE FINITE ELEMENT SIMULATION OF MAGNETIC COMPONENTS

In order to more intuitively verify the internal flux density and magnetic field intensity distribution of different magnetic components, the finite element simulation comparison of DM, DIM and NIM of DF-BC was compared out by using the finite element simulation software [18], [19]. The material of the magnetic core is PC40 from TDK. Considering the influence of temperature rise, the saturation magnetic density is about 0.35T. EE33 core is adopted as the high-frequency inductor of DM, the number of turns is 35, and the air gap is 0.8mm. The low-frequency inductor of DM is EE40 magnetic core, the number of turns is 60, and the air gap is 0.5mm. EE40 cores are adopted for both DIM and NIM, and the air gap is 1mm. For DIM, the turns of each column are taken as follows: $N_{\mathrm{I}} = N_{\mathrm{II}} = 31$, $N_{\mathrm{III}} = 83$. For NIM, the turns of each column are set as foll-ows: $N_{\mathrm{H}} = 50, N_{\mathrm{L1}} = 75$, $N_{\mathrm{L2}} = 29$.

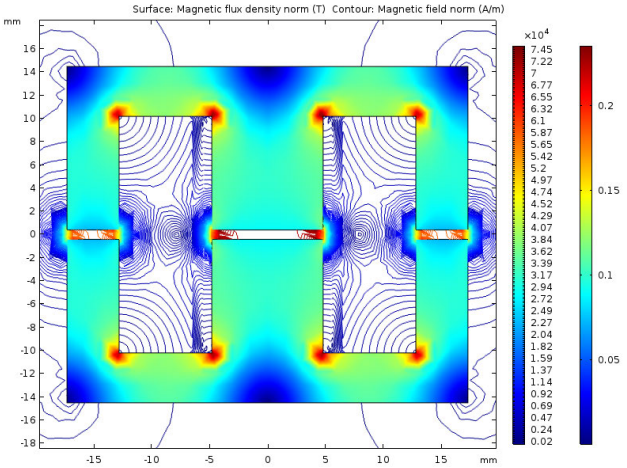

FIGURE 20. Simulation of high-frequency inductor of DM.

Figure 20 shows a finite element simulation of the DM high-frequency inductor, with a working magnetic flux destiny is about 0.18T. Figure 21 shows a finite element simulation of the DM low-frequency inductor with a working magnetic flux density is about 0.22T. The working magnetic flux density of DM is less than the saturation magnetic density of 0.35T. Figure 22 shows a finite element simulation of a DIM inductor with a working magnetic flux density of about 0.28T. Figure 23 shows a finite element simulation of a NIM inductor with a working magnetic flux density of about 0.22T. The working magnetic flux density of the two integration modes is less than the saturated magnetic density of 0.35T, which meet the normal operation requirements. However, DIM inductors lead to higher saturation of the right column of the EE magnetic core, and figure 22 clearly shows the lower utilization rates of other DIM magnetic columns. It can be clearly seen from figure 23 that NIM has lower saturation magnetic density and higher utilization of magnetic core than DIM. Therefore, compared with DIM, smaller magnetic

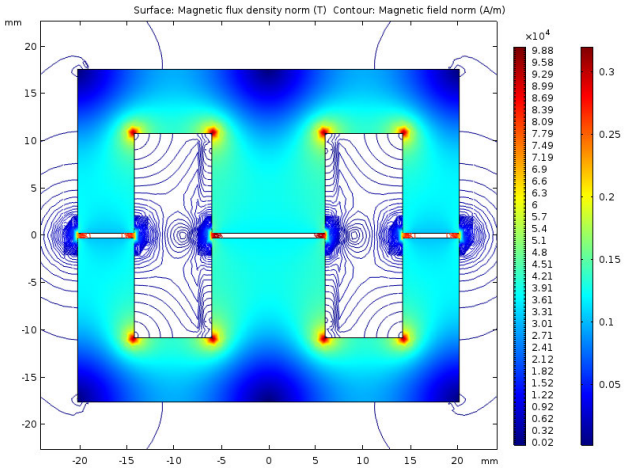

FIGURE 21. Simulation of low-frequency inductor of DM.

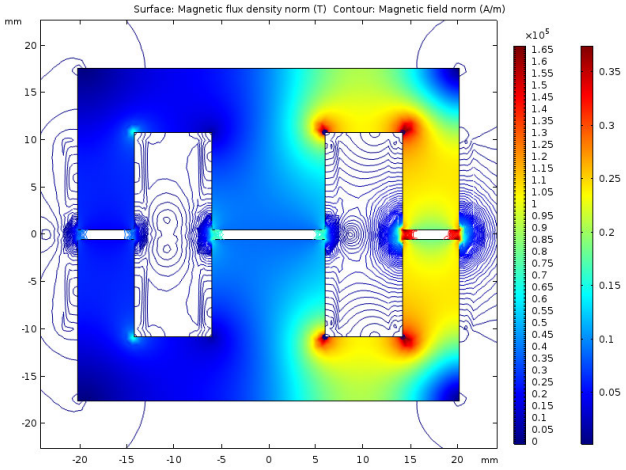

FIGURE 22. Simulation of DIM.

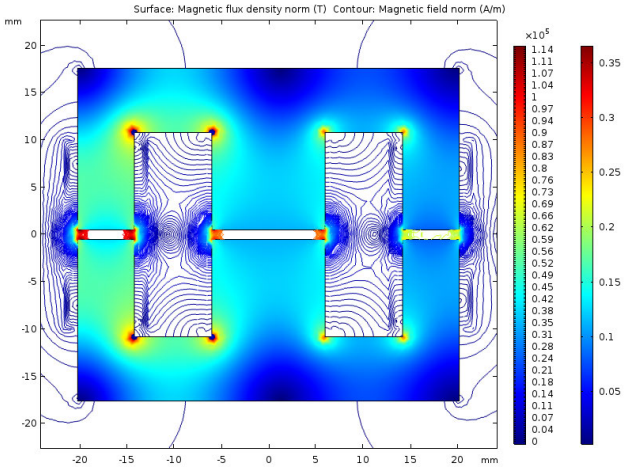

FIGURE 23. Simulation of NIM.

cores can be selected for NIM inductors to further reduce the magnetic components. This is also consistent with the previous analysis.

V. EXPERIMENTAL VERIFICATION

Based on the previous theoretical analysis, a 150W experimental prototype of a DF-BC was established. On the basis of the discrete inductor double-frequency buck circuit, only the discrete inductors are replaced with integrated inductors, and other parameters are kept unchanged. EE33 and EE40 are adopted as the DM high-frequency and the low-frequency inductor magnetic cores respectively, while EE40 is adopted as the magnetic core of NIM inductor. The DM and DIM parameters are consistent with the simulation. For NIM, theoretically, the NIM parameters should be the same as the simulation, but the leakage inductance of inductance coupling is independent of winding turns and related to the winding distance, while the two winding distances of high-frequency inductor and low-frequency inductor are different, so the coupling degree of high-frequency inductor and low-frequency inductor is different. The coupling coefficient of each winding when NIM turns are $N_{\mathrm{H}} = 50, N_{\mathrm{L1}} = 75, N_{\mathrm{L2}} = 29$ measured by digital bridge is shown in Table 6. In practical design, the most simple and accurate method is to calculate the turns ratio of the two windings of the low-frequency inductor by using the ratio of the coupling coefficient of the two windings of the high-frequency inductor and the low-frequency inductor, and then fine-tuning it. Finally, the actual number of turns in this article are $N_{\mathrm{H}} = 50$, $N_{\mathrm{L1}} = 75$, $N_{\mathrm{L2}} = 34$.

TABLE 6. NIM coupling coefficient of winding.

	L_{H}	L_{L1}	L_{L2}
L_{H}	×	0.0741	0.168
L_{L1}	0.0741	×	0.1354
L_{L2}	0.168	0.1354	×

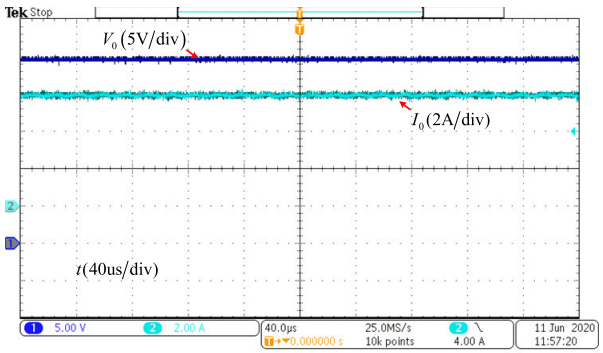

FIGURE 24. Steady-state output voltage and output current of DM.

Figure 24 shows the steady-state output voltage and output current of DM. Figure 25 shows the steady-state high-frequency and low-frequency inductor currents of DM, and figure 26 shows output voltage and current of DM when the

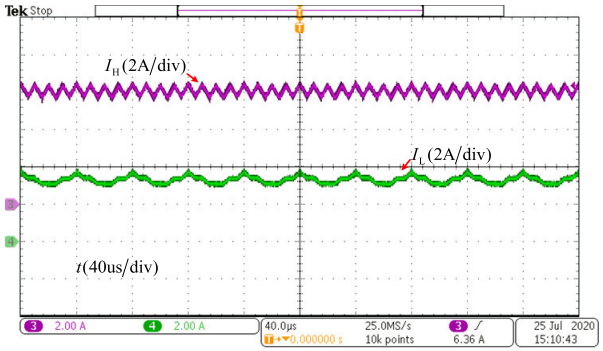

FIGURE 25. Steady-state high-frequency inductor current and low-frequency inductor current of DM.

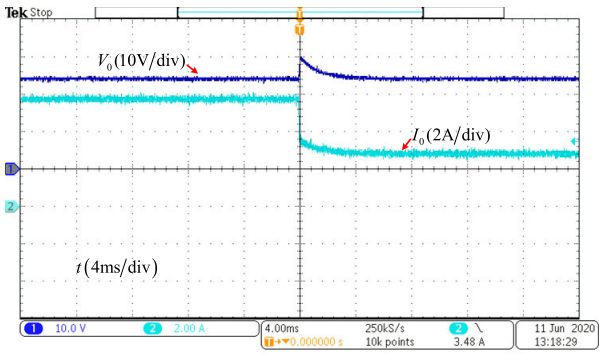

FIGURE 26. Output voltage and current of DM when the load jump.

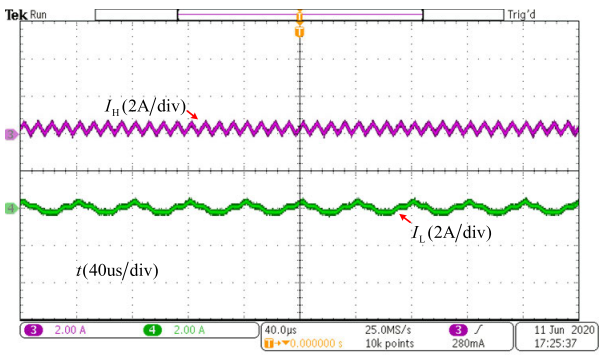

FIGURE 27. The inductor current in BCM of DM.

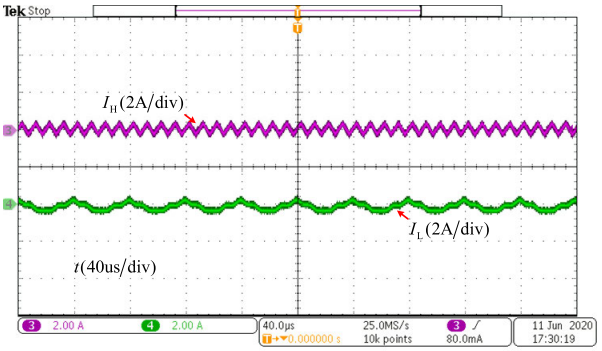

FIGURE 28. The inductor current in DCM of DM.

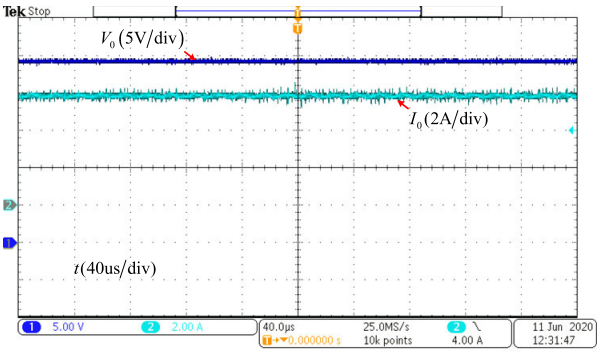

FIGURE 29. Steady-state output voltage and output current of NIM.

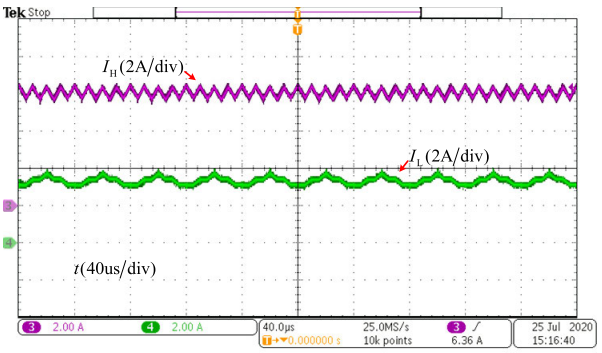

FIGURE 30. Steady-state high-frequency inductor current and low-frequency inductor current of NIM.

load change from full to half. Figure 27 and figure 28 show the inductor current of boundary conduction mode(BCM) and discontinuous conduction mode(DCM) of DM respectively. When operating in BCM and DCM modes, double-frequency converters can still play their shunt role.

Figure 29 shows the steady-state output voltage and output current of NIM. Figure 30 shows the steady-state high-frequency and low-frequency inductor currents of NIM, and figure 31 shows output voltage and current of NIM when the load changes from full to half. Figure 32 and figure 33 show the inductor current waveforms of BCM and DCM mode of NIM respectively.

By comparing the waveforms of DM and NIM, it can be seen that the high-frequency and low-frequency inductor current waveforms of the converter in steady state operation are basically the same as the analyzed before, and it is verified that the new integrated magnetic inductor achieves the same effect as the discrete magnetic component. When the load changes from full to half, as shown in figure 26 and figure 31, the output voltage and output current of the double-frequency converter are consistent before and after the magnetic integration. Whether in BCM or DCM mode, NIM can still achieve the same function as DM.

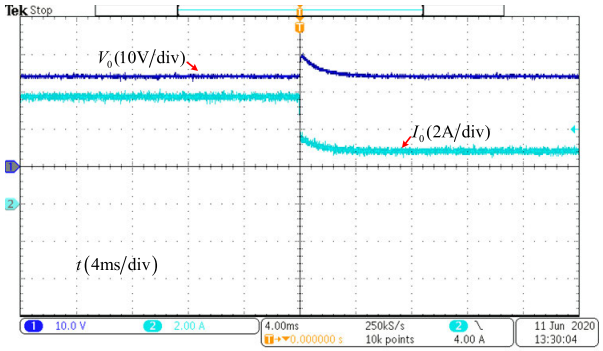

FIGURE 31. Output voltage and current of NIM when the load jump.

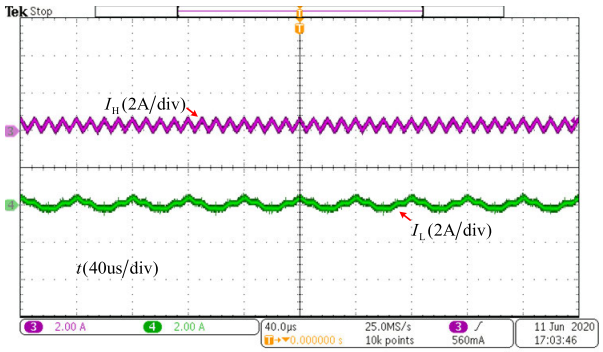

FIGURE 32. The inductor current in BCM of NIM.

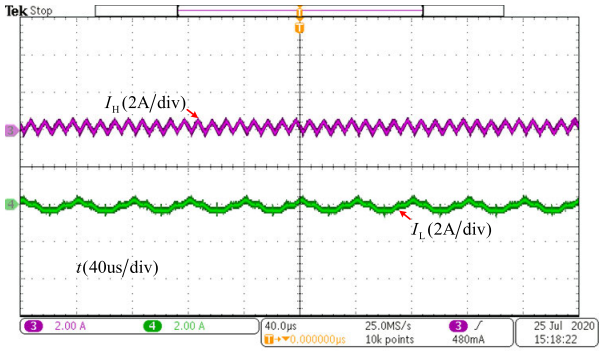

FIGURE 33. The inductor current in DCM of NIM.

Through measurement: compared with DM, NIM volume and weigh are reduced by 44% and 40.8% respectively, so as to improve power density. Figure 34 shows the efficiency comparison of the low-frequency 25kHz buck converter, the high-frequency 100kHz buck converter, the DM DF-BC and the NIM DF-BC under different output currents. As can be seen from figure 34: the efficiency of DM DF-BC is between the efficiencies of high-frequency converter and low-frequency converter, indicating that the double-frequency converter can reduce high-frequency switching losses. The efficiency of NIM DF-BC is close to that of DM DF-BC, verifying the effectiveness of the NIM structure. The loss comparison between DM and NIM is shown in figure 35.

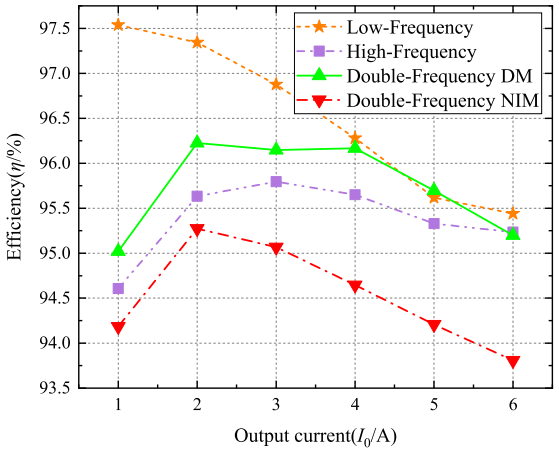

FIGURE 34. Efficiency comparison.

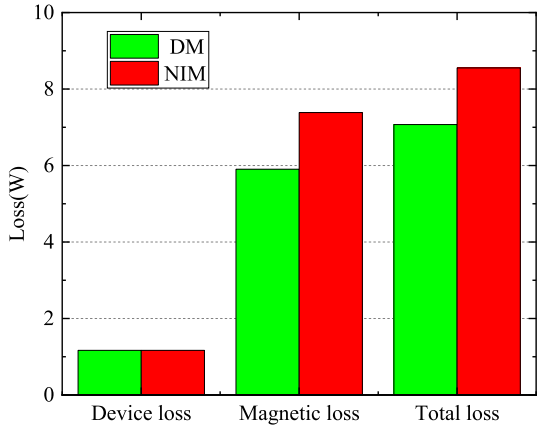

FIGURE 35. Loss comparison between DM and NIM.

Obviously, the extra loss of NIM than DM is mainly caused by the magnetic components, and the magnetic loss is mainly the core loss.

VI. CONCLUSION

In this article, a new type of magnetic integration double-frequency DC/DC converter was proposed to integrate two inductors with different working frequencies into the same magnetic core. After integration, the high-frequency and low frequency inductors operated efficiently and stably. Compared with DM, the volume and weight of the NIM were reduced by 44% and 40.8% respectively, which effectively improved the power density of the double-frequency converter and reduced the cost. Compared with the existing solutions of magnetic integration double-frequency DC/DC converter, this method can further increase the power density of the converter, and reduce the magnetic saturation of the magnetic integration components, thereby reducing the iron core loss, as well as improving the dynamic response of the low-frequency cell and hence reduce the switching loss. The double-frequency synchronous Buck converter can also work in the reverse state to achieve bidirectional flow of energy.

This method can also be applied to other converters. Finally, the correctness of the theoretical analysis is verified by a 150W experimental prototype.

REFERENCES

[1] C. Fei, F. C. Lee, and Q. Li, "High-efficiency high-power-density LLC converter with an integrated planar matrix transformer for high-output current applications," *IEEE Trans. Ind. Electron.*, vol. 64, no. 11, pp. 9072–9082, Nov. 2017.
[2] Z. Luowei, D. Xiong, F. Zhihong, and L. Quanming, "The Buck converter with double frequency," *Proc. CESS*, vol. 26, no. 6, pp. 68–72, 2006.
[3] D. Xiong, Z. Luowei, L. Quanming, and H. Shiying, "Relationship between circuit parameter and system performance of Buck converter with double frequency," *Trans. China Electrotech. Soc.*, vol. 20, no. 11, pp. 49–55, 2005.
[4] D. Xiong, Z. Luowei, H. Shiying, and L. Quanming, "A list of basic DC/DC converters with double-frequency," *Trans. China Electrotech. Soc.*, vol. 21, no. 5, pp. 24–28, 2006.
[5] Q. Chen, X. Ruan, and Y. Yan, "The application of the magnetic-integration techniques in switching power supply," *Trans. China Electrotech. Soc.*, vol. 19, no. 3, pp. 1–8, Mar. 2004.
[6] X. Du, L. Zhou, and H.-M. Tai, "Double-frequency buck converter," *IEEE Trans. Ind. Electron.*, vol. 56, no. 5, pp. 1690–1698, May 2009.
[7] F. Yang, X. Ruan, Y. Yang, and Z. Ye, "Interleaved critical current mode boost PFC converter with coupled inductor," *IEEE Trans. Power Electron.*, vol. 26, no. 9, pp. 2404–2413, Sep. 2011.
[8] W. Chen, F. C. Lee, X. Zhou, and P. Xu, "Integrated planar inductor scheme for multi-module interleaved quasi-square-wave (QSW) DC/DC converter," in *Proc. 30th Annu. IEEE Power Electron. Spec. Conf.*, vol. 2, Jul. 1999, pp. 759–762.
[9] P. Zumel, O. Garcia, J. A. Cobos, and J. Uceda, "Magnetic integration for interleaved converters," in *Proc. 18th Annu. IEEE Appl. Power Electron. Conf. Expo.*, Feb. 2003, pp. 1143–1149.
[10] P.-L. Wong, Q. Wu, P. Xu, B. Yang, and F. C. Lee, "Investigating coupling inductors in the interleaving QSW VRM," in *Proc. APEC. 15th Annu. IEEE Appl. Power Electron. Conf. Expo.*, Feb. 2000, pp. 759–763.
[11] D. K.-W. Cheng, L.-P. Wong, and Y.-S. Lee, "Design, modeling, and analysis of integrated magnetics for power converters," in *Proc. IEEE-PESC*, Jun. 2000, pp. 320–325.
[12] Z. Xiaofeng, Z. Luowei, L. Quanming, and L. Weiguo, "Double frequency DC/DC converter with magnetic integration," *Trans. China Electrotech. Soc.*, vol. 25, no. 1, pp. 77–83 and 89, 2010.
[13] D. Pan, X. Ruan, C. Bao, W. Li, and X. Wang, "Magnetic integration of the LCL filter in grid-connected inverters," *IEEE Trans. Power Electron.*, vol. 29, no. 4, pp. 1573–1578, Apr. 2014.
[14] S. Vijayalakshmi and T. S. R. Raja, "Development of robust discrete controller for double frequency buck converter," *Automatika*, vol. 56, no. 3, pp. 303–317, Jan. 2015.
[15] V. Shirmohammadli, A. Saberkari, and E. Alarcon, "Performance analysis of dual-frequency buck converter for integrated power management," in *Proc. 5th Annu. Int. Power Electron., Drive Syst. Technol. Conf. (PEDSTC)*, Feb. 2014, pp. 402–407.
[16] Z. Lu, W. Chen, and C. Mao, "Analysis of integrated magnetics using near-field coupling in DC/DC converter with current doubler rectifier," *Trans. China Electrotech. Soc.*, vol. 26, no. 11, pp. 92–98, 2011.
[17] Q. Chen, L. Xu, Z. Li, X. Ren, and X. Ruan, "Improved gyrator-capacitor simulation model of nonlinear magnetic core," *Trans. China Electrotech. Soc.*, vol. 24, no. 4, pp. 14–21, 2009.
[18] S. Wang, D. Yuan, A. Wang, K. Liu, H. Li, and S. Wang, "Circuit-field coupling and magnetic-thermal coupling analysis of RRF converter designed with magnetic integration," *IEEE Trans. Magn.*, vol. 55, no. 5, pp. 1–8, May 2019.
[19] D. Huang, S. Ji, and F. C. Lee, "LLC resonant converter with matrix transformer," *IEEE Trans. Power Electron.*, vol. 29, no. 8, pp. 4339–4347, Aug. 2014.

SHENGWEI GAO was born in Tianjin, China, in 1978. He received the B.S., M.S., and Ph.D. degrees in electrical engineering from the Hebei University of Technology, in 2005 and 2011, respectively.

He completed his Postdoctoral work at the School of Mechanical Electronics, Tiangong University, in 2019. From 2005 to 2011, he was a Lecturer with the School of Electrical Engineering and Automation, Tiangong University. Since 2011, he has been an Assistant Professor with the Electrical Engineering and Automation Department, Tiangong University. He is the author of one book, more than 50 articles, and more than 20 inventions. His research interests include power electronic transformation technology and application and embedded system design and application.

Dr. Gao was a recipient of the Outstanding Young Teacher Award of Tianjin, in 2011, the SANG MA TRUSE FUND of HongKong, and the First Prize of Teaching Achievement of Tianjin Municipal Government, in 2019.

HAO WANG was born in Shandong, China, in 1995. He received the B.S. degree in electrical engineering from the University of Jinan, Jinan, Shandong, China, in 2017. He is currently pursuing the M.S. degree in electrical engineering with Tiangong University, Tianjin, China. His current research interests include power electronics converter technology and its magnetic technology, and the application of GaN HEMT in dc/dc converter.